Research Article | Vol. 29, No. 23 / 8 Nov 2021 / Optics Express 38044
Optics EXPRESS

Efficient polarization splitter-rotator on thin-film lithium niobate

XUANHAO WANG,[1] AN PAN,[1] TINGAN LI,[1] CHENG ZENG,[1,2] AND JINSONG XIA[1,3]

[1]Wuhan National Laboratory for Optoelectronics, Huazhong University of Science and Technology, Wuhan 430074, China
[2]zengchengwuli@hust.edu.cn
[3]jsxia@hust.edu.cn

Abstract: Recently, thin-film lithium niobate coherent modulators have emerged as a promising candidate for the next generation coherent communication system. High performance polarization splitter-rotators (PSRs) are essential to further achieve dual polarization coherent modulators. Here we present a PSR on the lithium niobate on insulator (LNOI) platform with the measured insertion loss less than 1 dB, extinction ratio exceeding 26.6 dB and 19.6 dB for TE0 and TM0 modes, working bandwidth of 1520–1580 nm and total length of 440 μm. In addition, a relatively large fabrication tolerance for waveguide width is also proved. This demonstrated PSR can find its potential application in polarization-division multiplexing (PDM) optical transmitter based on LNOI.

© 2021 Optica Publishing Group under the terms of the Optica Open Access Publishing Agreement

1. Introduction

Thin film Lithium niobate (LN) platform is considered as a promising solution for the next generation of photonic integrated circuits (PICs). With the development of LN dry etching technique, a series of outstanding photonic devices were fabricated based on LNOI [1–6]. The electro-optic modulator is one of the most attractive devices due to the potential for using in high speed optical communication system. Wang et al. demonstrated a revolutionary electro-optic modulator on LNOI with 45 GHz bandwidth and 1.4 V half-wave voltage [7]. Then Xu et al. further showed the first coherent optical modulator based on LNOI platform, supporting modulation data rate up to 320 Gb s^{-1} [8]. PDM technology is widely used in Si and InP-based coherent transceivers to efficiently increase communication capacity when single-channel data transmission speed reaches the bottleneck [9,10]. For LNOI platform, the IQ modulator with an external PDM emulator was successfully demonstrated, which achieves a data rate of 1.58 Tb s^{-1} on a single wavelength [11]. Considering the size and stability of the coherent optical transmitter, the function of PDM must be realized on chip. PSR combining the functions of polarization beam splitting and rotation is the core device for PDM technology. Recently, there have been some reports for PSR on LNOI platform [12,13]. However, high-performance PSRs are still lack and urgently demanded for LNOI platform.

Most of the PSRs are researched on silicon on insulator (SOI) platform. The principles of the reported PSRs are commonly described as mode coupling and mode evolution. In mode coupling based PSRs, vertical or horizontal symmetry is broken to ensure that cross-polarization coupling can occur. Several types of PSRs are achieved based on the modified directional couplers(DCs), such as bent DC [14] and double-etched DC [15,16]. Mode coupling based PSRs have compact size, but they are not suitable for practical products due to narrow working bandwidth and complex fabrication processes. Mode evolution based PSRs are usually composed of a mode evolution taper and an asymmetrical directional coupler (ADC) [17–19]. The mode evolution taper realizes the conversion of TM0 to TE1 mode while TE0 mode unchanged. Then the TE0 and TE1 modes are separated by ADC and the TE1 mode couples to TE0 mode simultaneously.

#443798 https://doi.org/10.1364/OE.443798
Journal © 2021 Received 22 Sep 2021; revised 22 Oct 2021; accepted 23 Oct 2021; published 29 Oct 2021

Optics EXPRESS

The advantages of mode evolution based PSRs are simple single-step etching, but the working bandwidth and fabrication tolerance are still limited due to the precise phase matching conditions of the ADC. In order to solve this problem, asymmetric Y-junction is proposed as a TE0-TE1 mode sorter [20–22]. The unique mode-sorting characteristic of the asymmetric Y-junction is based on adiabatic mode evolution, which means inherently weak wavelength dependence and insensitivity of fabrication errors. The asymmetric Y-junction has been proven to achieve PSR on SOI platform, but it is never realized on LNOI.

In this paper, we demonstrate a PSR based on LNOI platform, which cascades an adiabatic taper and an asymmetric Y-junction. The insertion loss is less than 1 dB for both polarizations of the entire C-band. In the wavelength span of 1520–1580 nm, the extinction ratios exceed 26.6 dB and 19.6 dB for TE0 and TM0 modes, respectively. Moreover, the performance degradation caused by fabrication error is analyzed, showing that the PSR has a relatively large fabrication tolerance.

2. Design and simulation

The schematic structure of the demonstrated PSR is shown in Fig. 1(a) and 1(b). It consists of an adiabatic taper and an asymmetric Y-junction. The adiabatic taper is used to convert the launched TM0 mode to TE1 mode due to mode hybridization phenomenon [23]. In order to reduce the size of PSR, the adiabatic taper is divided into three segments. The first and third tapers serve as the connection with input single-mode waveguide and asymmetric Y-junction. The second taper is the core part to realize mode conversion. The asymmetric Y-junction with a small divergence angle can act as a mode sorter. An input mode will evolve to the mode of output arm with the closest effective index [22], which means input TE0 and TE1 modes can evolve into TE0 mode in wide and narrow arm, respectively. As analyzed above, the function of PSR can be achieved by cascading adiabatic taper and asymmetric Y-junction. The input TM0 mode is first converted to TE1 mode through the adiabatic taper and subsequently evolves to TE0 mode and outputs from port 2. On the other hand, the input TE0 mode maintain propagating in the device and outputs from port 1. The demonstrated PSR is designed on the X-cut LNOI with top LN film thickness of 500 nm, and lights travel along Y-axis of LN. The refractive index of LN is $n_o = 2.234$ and $n_e = 2.169$, respectively. The device is based on LN ridge waveguide with etching depth $H_e = 260$ nm, and the 70°-sidewall angle is caused by the fabrication processes. The cross-section of the waveguide is shown in Fig. 1(c), which has a SiO_2 cladding and sits on top of 4.7 μm thick silica ($n = 1.46$).

Thanks to the structure of ridge waveguide for breaking the vertical symmetry, mode hybridization can be accomplished in the adiabatic taper. Figure 2(a) shows the calculated effective refractive indices of the eigenmodes as the LN ridge waveguide width (W_{wg}) varies by a Finite Difference Eigenmode (FDE) solver (LUMERICAL). The mode hybridization of TM0 and TE1 modes obviously appears around $W_{wg} = 2.55$ μm, as shown in the dashed circle of Fig. 2(a). The mode conversion between TM0 and TE1 modes will occur when light propagates along an adiabatic taper whose end widths cover the mode hybridization region. The end widths of the second taper are thus set to be $W_1 = 2.45$ μm and $W_2 = 2.6$ μm, respectively. $W_0 = 1$ μm is set to ensure single mode input waveguide and $W_3 = 3$ μm is set to stay away from mode hybridization region. The Eigenmode Expansion (EME) solver (LUMERICAL) is used to simulate the adiabatic taper. The lengths of the first and third taper won't influence the mode conversion greatly. For any given value of L1 and L3, the taper length of the second taper can be optimized to achieve a high mode conversion efficiency [18]. The lengths of the first and third taper are chosen as $L_1 = 100$ μm and $L_3 = 100$ μm, respectively. Figure 2(b) shows the calculated mode conversion efficiency as the second taper length L_2 varies at the wavelength of 1550 nm. It can be seen that the conversion efficiency of TM0 to TE1 mode increases as L_2 increases. There are some fluctuations of the conversion efficiency, which can be suppressed by increasing L_1

Optics EXPRESS

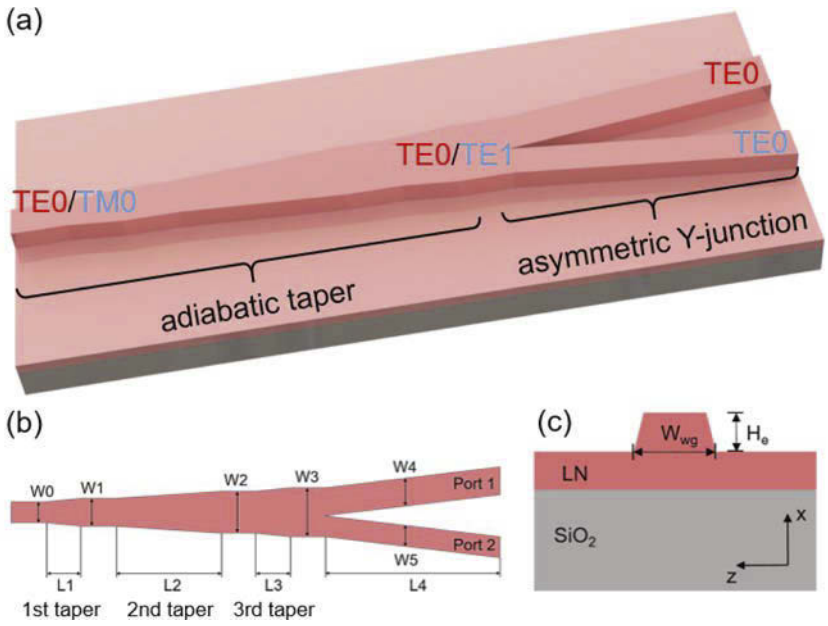

Fig. 1. (a) Schematic structure of the PSR. (b) Top view of the PSR. (c) Cross section view of LN waveguides.

and L_3 [18]. However, we can choose an appropriate value of L_2 to achieve high conversion efficiency without increasing the device size. L_2 is set to be 140 μm, where TM0 to TE1 mode conversion efficiency is 99.93%. On the other hand, input TE0 mode doesn't change through the adiabatic taper. The input TE0 and TM0 light propagations through the taper at the wavelength of 1550 nm are shown in Fig. 2(c-d), respectively.

The asymmetric Y-junction is used to separate TE0 and TE1 modes. When TE0 mode inputs, it will evolve to TE0 mode in the wide arm for the reason that the effective refractive indices of the two modes are closest. Similarly, the input TE1 mode will evolve to TE0 mode in the narrow arm when choosing the suitable widths of the output arms. The output arm widths are set to be $W_4 = 1.7$ μm and $W_5 = 1.3$ μm to meet the above conditions. This phenomenon only occurs when the device is adiabatic, which means that the divergence angle between the output arms should be very small. The distance of two asymmetric Y-junction arm ends is fixed as 1μm. The EME solver is also used to optimize the asymmetric Y-junction and the simulated results are shown in Fig. 3. Figure 3(a-b) show the mode conversion efficiency as the output arm length L_4 varies. When setting $L_4 = 86$ μm, the mode conversion efficiency between input TE0 mode and TE0 mode in port 1 is 98.56%, while that between input TE1 mode and TE0 mode in port 2 is 99.03%. After optimization, the simulated light propagations are shown in Fig. 3(c-d) when TE0 and TE1 modes are launched, respectively.

Combining the adiabatic taper and asymmetric Y-junction, PSR is finally achieved. The light propagations through the complete PSR are simulated by a 3D finite-difference-time-domain (FDTD) solver (LUMERICAL). From Fig. 4(a) and 4(b), it can be seen that the input TE0 mode remains unchanged in the adiabatic taper, then just evolves into TE0 mode and exports from port 1. On the other hand, the input TM0 mode is first converted to TE1 mode after the adiabatic taper. The TE1 mode then evolves into TE0 mode and exports from port 2 of the asymmetric Y-junction. Figure 4(c) and 4(d) show the calculated transmission ratios at output ports when TE0 and TM0 modes input, respectively. In the wavelength span of 1500–1600 nm, the PSR shows good performance with insertion loss less than 0.08 dB and

Optics EXPRESS

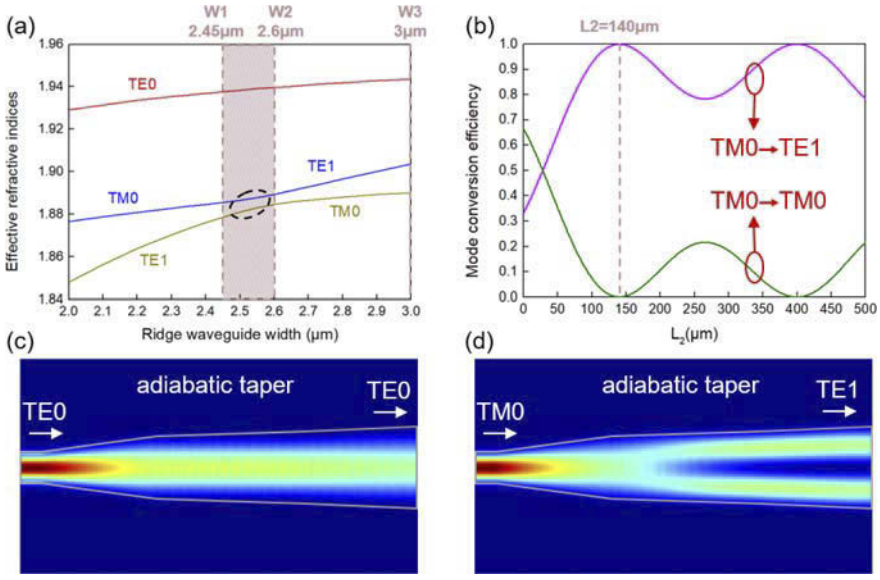

Fig. 2. (a) Effective refractive indices of the eigenmodes in LN waveguide as a function of the ridge width W_{wg}. (b) The mode conversion efficiency of TM0 to TE1 mode and TM0 to TM0 mode as a function of the second taper length L2. The light propagations through the adiabatic taper under (c) TE0 mode input and (d) TM0 mode input.

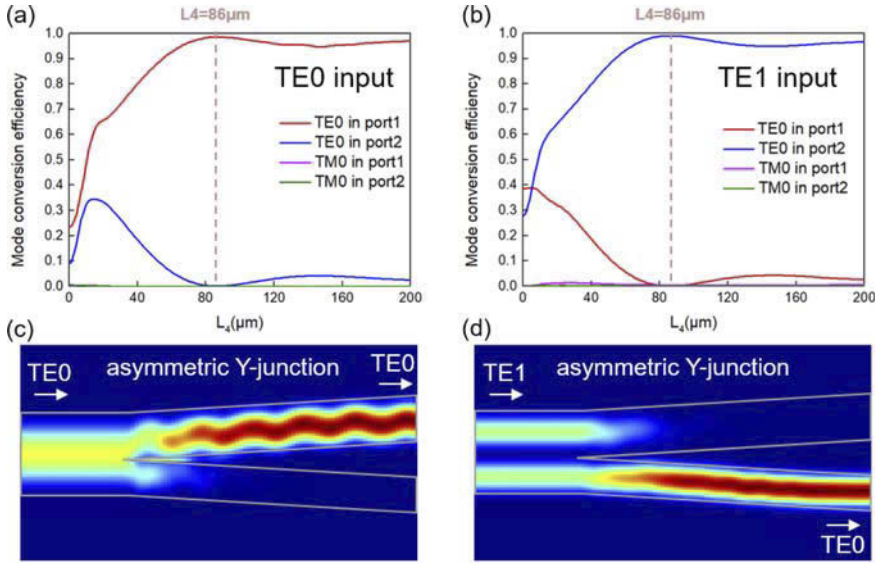

Fig. 3. The mode conversion efficiency as a function of the asymmetric Y-junction arm length L4 under (a) TE0 mode input and (b) TE1 mode input. (c) The light propagations through the asymmetric Y-junction under (a) TE0 mode input and (d) TE1 mode input.

extinction ratio larger than 26.8 dB for TE polarization. When TM0 mode inputs, we can get a wavelength range of 1510–1585 nm with insertion loss less than 0.2 dB and extinction ratio larger than 20 dB.

Optics EXPRESS

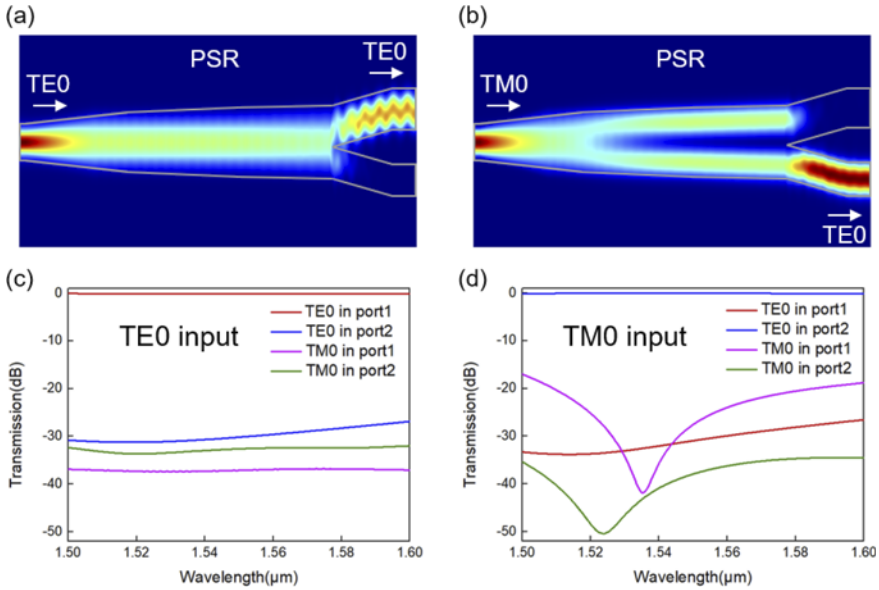

Fig. 4. (a) The light propagations through the PSR under (a) TE0 mode input and (b) TM0 mode input. The transmission ratio as a function of the wavelength under (c) TE0 mode input and (d) TM0 mode input.

3. Fabrication and measurement

The demonstrated PSR is fabricated on a commercial X-cut LNOI wafer (NANOLN). The pattern is defined by electron beam lithography (EBL) process and transferred onto 180 nm chrome film deposit by electron-beam evaporation (EBE) process. Then the patterned chrome is used as the mask to etch LN by argon-based inductively coupled plasma reactive-ion-etching (ICP-RIE) process. Finally, the remaining chrome mask is removed by chromium etchant and a silica cladding with the thickness of 1 μm is deposited by plasma enhanced chemical vapor deposition (PECVD) process. Detailed fabrication process is discussed in Supplement 1. The grating couplers are used to inject light into and out of the chip for measurement. Meanwhile the grating couplers play a role as polarizers due to the significant polarization dependence, thus TE-type and TM-type grating couplers are designed, respectively. The etching depth of the grating couplers is designed to be the same with waveguides in order to simplify the fabrication processes. The period and duty cycle of the TE-type grating couplers are 0.98 μm and 0.54, respectively, and the period and duty cycle of the TM-type grating couplers are 1.15 μm and 0.5, respectively. The measured coupling losses of TE-type and TM-type grating couplers are 6.15 dB and 8.65 dB at 1550 nm, respectively. The polarization extinction ratios of both grating couplers are larger than 17 dB. TE or TM mode light can be coupled into the chip by selecting the corresponding type of grating couplers. Detailed measurement methods and results of grating couplers are discussed in Supplement 1. Figure 5 shows the microscope images and partially enlarged scanning electron microscope (SEM) image of the fabricated PSR. The measurement strategies are shown in Fig. 5(a). For TE0 mode input, TE-type grating couplers are selected for all output ports of the PSR, because there is no polarization change through the light path. As for TM0 mode input, TM-type grating coupler is put at port 1 because the remaining TM0 mode determines the extinction ratio of the device as shown in Fig. 4(d). TE-type grating coupler is used at port 2 to measure the conversion loss from TM0 to TE0 mode. The total length of the PSR is 440 μm, which is much smaller than LN Mach–Zehnder interferometer modulators.

Optics EXPRESS

Therefore, the PSR and modulator can be easily monolithically integrated on LNOI for PDM optical transmitter. In the measurement, we connect two S-bend waveguides behind the port 1 and port 2 to increase the gap between two output grating couplers.

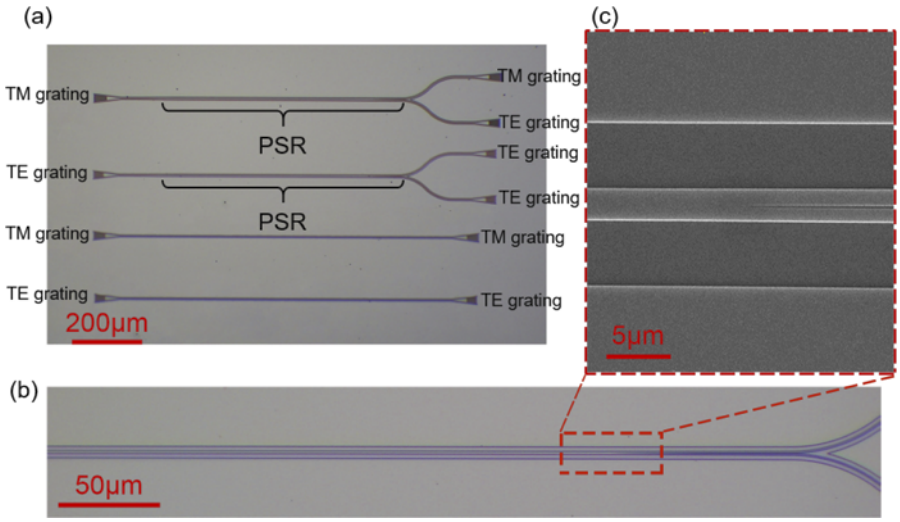

Fig. 5. (a) Microscope image of the fabricated PSR and grating coupler. (b) Microscope image of the fabricated PSR. (c) SEM image of part asymmetric Y-junction.

A tunable laser (Santec TLS-510) is used during the measurement and a polarization controller (PC) is put behind the laser to adjust the polarization state. The light beam enters and exits the chip through the vertical coupling system. The output light of the chip is collected by an optical power meter (YOKAGAWA AQ2211). Figure 6(a) and 6(b) show the measured and simulated normalized transmission spectra of the PSR by scanning the wavelength from 1520 nm to 1580 nm. The insertion loss is less than 1 dB in the entire C-band when both TE0 and TM0 modes input. It can be seen from Fig. 6(a) that the transmission spectra of port 1 at long wavelength are slightly larger than 0 dB, for the reason that the losses of the fabricated grating couplers for reference and measurement are not exactly the same. The extinction ratio larger than 26.6 dB is achieved from 1520 to 1580 nm when TE0 mode inputs. When TM0 mode mode inputs, the extinction ratio is larger than 19.6 dB in the same wavelength band. These results show that the measured and simulated results are in good agreement.

We further investigate the fabrication tolerance of the PSR. A series of devices are fabricated on the same chip with waveguide width varying in a step of 20 nm. The insertion loss and extinction ratio at 1550 nm as the waveguide width varies are shown in Fig. 6(c) and 6(d). For TE0 mode input, the insertion loss is less than 0.3 dB and extinction ratio is larger than 21 dB as the waveguide width varying in a range of −80 nm to 100 nm. The fabrication errors have a more obvious impact on device performance for TM0 mode input. Within −20nm to 40nm waveguide width deviation, the insertion loss is less than 0.9 dB and extinction ratio is large than 20 dB. The 60 nm fabrication tolerance can be accepted by EBL and deep ultraviolet lithography processes [24].

Table 1 summarizes several recent works on PSRs. Among all these PSRs, the fabrication tolerance of our device is the largest, which benefits from the working principle of mode evolution. The insertion loss, bandwidth and extinction ratio all reach the mainstream level. Therefore, the performance of our PSR is relatively balanced and can meet the requirements of PDM coherent optical transmitters.

Optics EXPRESS

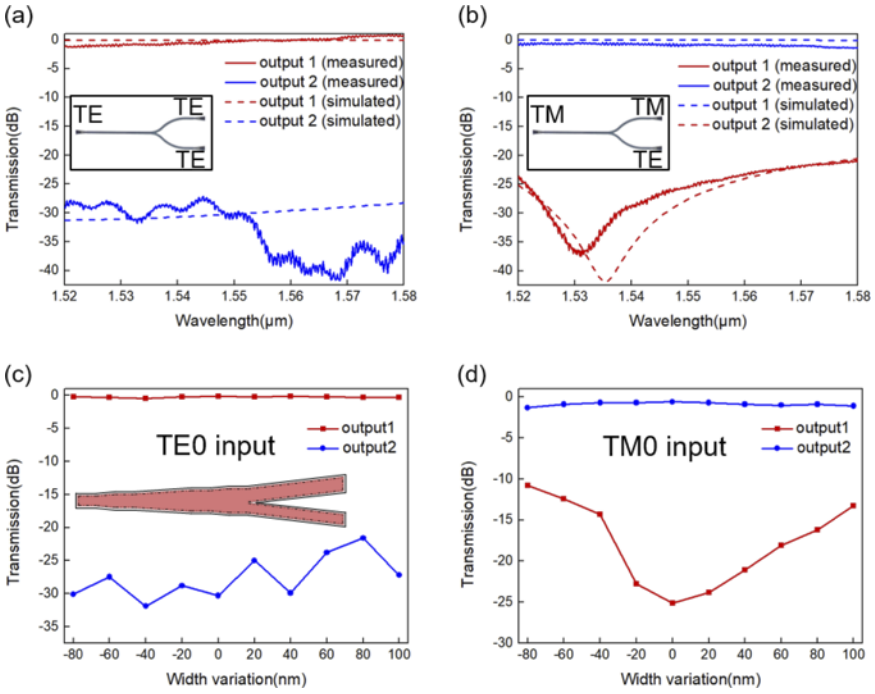

Fig. 6. Measured transmission spectra of the PSR under (a) TE0 mode input and (b) TM0 mode input. Inserts: the measurement strategy of TE0 and TM0 mode input PSRs. Measured transmission responses at 1550 nm as waveguide width varying under (c) TE0 mode input and (d) TM0 mode input. The insert in (c) shows the waveguide width deviation.

Table 1. Comparison of several PSRs

Structures	Insertion loss (dB)	Extinction ratio (dB)	Bandwidth (nm)	Tolerance (nm)
Bent DC [14]	<1	>18	41	20[a]
Double-etched DC [16]	<0.5	>20	30	10[a]
Taper with ADC [17]	<1.5	>20	50	\
Taper with ADC and bent DC filter [19]	<0.57	>20	85	\
Taper with asymmetric Y-junction [20]	<0.4[a]	>12[a]	400[a]	110[a]
This work	<1	>19.6	>60	60

[a]Simulation results.

4. Conclusion

In this paper, we demonstrate an on chip PSR based on LNOI, which cascades an adiabatic taper and an asymmetric Y-junction. The demonstrated PSR is fabricated by standard semiconductor processes with only single-step etching. The measurement results show low loss, high extinction ratio, broad working bandwidth and large fabrication tolerance of the PSR. The insertion loss less than 1 dB of the entire C-band is achieved for both TE0 and TM0 mode. From 1520 nm to 1580 nm, the extinction ratios exceed 26.6 dB and 19.6 dB for TE0 and TM0 mode, respectively. A relatively large fabrication tolerance for waveguide width is also proved, the extinction ratios remain larger than 20 dB at 1550 nm for both polarizations within −20nm to 40nm waveguide width deviation. The demonstrated PSR is a supplement for photonic devices on LNOI, and

Optics EXPRESS

can find its applications in PDM optical transmitters, polarization diversity circuits and on chip polarization controllers, etc.

Funding. National Key Research and Development Program of China (2019YFB2203800); National Natural Science Foundation of China (61835008, 61905079, 61905084).

Acknowledgments. We thank the Center of Micro-Fabrication and Characterization (CMFC) of WNLO and the Center for Nanoscale Characterization & Devices (CNCD), WNLO of HUST for the facility support.

Disclosures. The authors declare no conflicts of interest.

Data availability. Data underlying the results presented in this paper are not publicly available at this time but may be obtained from the authors upon reasonable request.

Supplemental document. See Supplement 1 for supporting content.

References

1. M. Zhang, C. Wang, R. Cheng, A. Shams-Ansari, and M. Lončar, "Monolithic ultra-high-Q lithium niobate microring resonator," Optica **4**(12), 1536–1537 (2017).
2. M. He, M. Xu, Y. Ren, J. Jian, Z. Ruan, Y. Xu, S. Gao, S. Sun, X. Wen, L. Zhou, L. Liu, C. Guo, H. Chen, S. Yu, L. Liu, and X. Cai, "High-performance hybrid silicon and lithium niobate Mach–Zehnder modulators for 100 Gbit s −1 and beyond," Nat. Photonics **13**(5), 359–364 (2019).
3. C. Hu, A. Pan, T. Li, X. Wang, Y. Liu, S. Tao, C. Zeng, and J. Xia, "High-efficient coupler for thin-film lithium niobate waveguide devices," Opt. Express **29**(4), 5397–5406 (2021).
4. J. Zhao, C. Ma, M. Rüsing, and S. Mookherjea, "High Quality Entangled Photon Pair Generation in Periodically Poled Thin-Film Lithium Niobate Waveguides," Phys. Rev. Lett. **124**(16), 163603 (2020).
5. A. Honardoost, K. Abdelsalam, and S. Fathpour, "Rejuvenating a Versatile Photonic Material: Thin-Film Lithium Niobate," Laser Photonics Rev. **14**(9), 2000088 (2020).
6. A. Boes, B. Corcoran, L. Chang, J. Bowers, and A. Mitchell, "Status and Potential of Lithium Niobate on Insulator (LNOI) for Photonic Integrated Circuits," Laser Photonics Rev. **12**(4), 1700256 (2018).
7. C. Wang, M. Zhang, X. Chen, M. Bertrand, A. Shams-Ansari, S. Chandrasekhar, P. Winzer, and M. Lončar, "Integrated lithium niobate electro-optic modulators operating at CMOS-compatible voltages," Nature **562**(7725), 101–104 (2018).
8. M. Xu, M. He, H. Zhang, J. Jian, Y. Pan, X. Liu, L. Chen, X. Meng, H. Chen, Z. Li, X. Xiao, S. Yu, S. Yu, and X. Cai, "High-performance coherent optical modulators based on thin-film lithium niobate platform," Nat. Commun. **11**(1), 3911 (2020).
9. S. Yamanaka, Y. Ikuma, T. Itoh, Y. Kawamura, K. Kikuchi, Y. Kurata, M. Jizodo, T. Jyo, S. Soma, M. Takahashi, K. Tsuzuki, M. Nagatani, Y. Nasu, A. Matsushita, and T. Yamada, "Silicon Photonics Coherent Optical Subassembly with EO and OE Bandwidths of Over 50 GHz," in *Optical Fiber Communication Conference 2020*, paper Th4A.4.
10. V. Lal, P. Studenkov, T. Frost, H. Tsai, B. Behnia, J. Osenbach, S. Wolf, R. Going, S. Porto, R. Maher, H. Hodaei, J. Zhang, C. Di Giovanni, K. Hoshino, T. Vallaitis, B. Ellis, J. Yan, K. Fong, E. Sooudi, M. Kuntz, S. Buggaveeti, D. Pavinski, S. Sanders, Z. Wang, G. Hoefler, P. Evans, S. Corzine, T. Butrie, M. Ziari, F. Kish, and D. Welch, "1.6Tbps Coherent 2-Channel Transceiver Using a Monolithic Tx/Rx InP PIC and Single SiGe ASIC," in *Optical Fiber Communication Conference 2020*, paper M3A.2.
11. X. Chen, G. Raybon, D. Che, J. Cho, and K. W. Kim, "Transmission of 200-GBaud PDM Probabilistically Shaped 64-QAM Signals Modulated via a 100-GHz Thin-film LiNbO3 I/Q Modulator," in *Optical Fiber Communications Conference 2021*, paper F3C.5.
12. L. Zhang, S. Yang, G. Zhang, X. Fu, L. Zhang, and L. Yang, "Broadband 2×2 Polarization Splitter-Rotator Based on an Adiabatic Asymmetric Directional Coupler on the Lithium-Niobate-on-Insulator," in *Asia Communications and Photonics Conference 2020*, paper M4A.176.
13. J. Y. Zhaoxi CHEN, Wing-Han Wong, Edwin Pun, and Cheng Wang, "Broadband adiabatic polarization rotator-splitter based on lithium niobate on insulator platform," Photon. Res., doc. ID 432906 (posted 29 September 2021, in press).
14. Y. Zhang, Y. He, X. Jiang, B. Liu, C. Qiu, Y. Su, and R. A. Soref, "Ultra-compact and highly efficient silicon polarization splitter and rotator," Apl Photonics **1**(9), 091304 (2016).
15. Y. Xiong, D.-X. Xu, J. H. Schmid, P. Cheben, S. Janz, and W. N. Ye, "Fabrication tolerant and broadband polarization splitter and rotator based on a taper-etched directional coupler," Opt. Express **22**(14), 17458–17465 (2014).
16. H. Guan, A. Novack, M. Streshinsky, R. Shi, Q. Fang, A. E.-J. Lim, G.-Q. Lo, T. Baehr-Jones, and M. Hochberg, "CMOS-compatible highly efficient polarization splitter and rotator based on a double-etched directional coupler," Opt. Express **22**(3), 2489–2496 (2014).
17. D. Dai and H. Wu, "Realization of a compact polarization splitter-rotator on silicon," Opt. Lett. **41**(10), 2346–2349 (2016).
18. D. Dai and J. E. Bowers, "Novel concept for ultracompact polarization splitter-rotator based on silicon nanowires," Opt. Express **19**(11), 10940–10949 (2011).
19. H. Xu and Y. Shi, "Ultra-broadband silicon polarization splitter-rotator based on the multi-mode waveguide," Opt. Express **25**(15), 18485–18491 (2017).

Optics EXPRESS

20. J. Wang, B. Niu, Z. Sheng, A. Wu, W. Li, X. Wang, S. Zou, M. Qi, and F. Gan, "Novel ultra-broadband polarization splitter-rotator based on mode-evolution tapers and a mode-sorting asymmetric Y-junction," Opt. Express **22**(11), 13565–13571 (2014).
21. H.-C. Chung and S.-Y. Tseng, "Ultrashort and broadband silicon polarization splitter-rotator using fast quasiadiabatic dynamics," Opt. Express **26**(8), 9655–9665 (2018).
22. N. Riesen and J. D. Love, "Design of mode-sorting asymmetric Y-junctions," Appl. Opt. **51**(15), 2778–2783 (2012).
23. A. Pan, C. Hu, C. Zeng, and J. Xia, "Fundamental mode hybridization in a thin film lithium niobate ridge waveguide," Opt. Express **27**(24), 35659–35669 (2019).
24. K. Luke, P. Kharel, C. Reimer, L. He, M. Loncar, and M. Zhang, "Wafer-scale low-loss lithium niobate photonic integrated circuits," Opt. Express **28**(17), 24452–24458 (2020).

202.119.43.156 {ts '2021-11-15 10:53:06'}